Photochemistry

Zitierweise: *Angew. Chem. Int. Ed.* **2020**, *59*, 22554 – 22562
Internationale Ausgabe: doi.org/10.1002/anie.202004701
Deutsche Ausgabe: doi.org/10.1002/ange.202004701

Unravelling Structural Dynamics within a Photoswitchable Single Peptide: A Step Towards Multimodal Bioinspired Nanodevices

Xinjiani Chen[+], Yuan Qi Yeoh[+], Yanbin He[+], Chenguang Zhou, John R. Horsley, Andrew D. Abell, Jingxian Yu* und Xuefeng Guo**

Dedicated to Professor Youqi Tang on the occasion of his 100th birthday

Abstract: *The majority of the protein structures have been elucidated under equilibrium conditions. The aim herein is to provide a better understanding of the dynamic behavior inherent to proteins by fabricating a label-free nanodevice comprising a single-peptide junction to measure real-time conductance, from which their structural dynamic behavior can be inferred. This device contains an azobenzene photoswitch for interconversion between a well-defined cis, and disordered trans isomer. Real-time conductance measurements revealed three distinct states for each isomer, with molecular dynamics simulations showing each state corresponds to a specific range of hydrogen bond lengths within the cis isomer, and specific dihedral angles in the trans isomer. These insights into the structural dynamic behavior of peptides may rationally extend to proteins. Also demonstrated is the capacity to modulate conductance which advances the design and development of bioinspired electronic nanodevices.*

Introduction

All proteins are dynamic structures that are in continuous motion,[1] with atoms undergoing random thermal fluctuations and small conformational changes by virtue of their local environment.[2] In the majority of cases, their function is determined by well-defined secondary structures,[3] such as helices and β-strands, but in a growing number of cases, cellular function has been shown to be defined by a disordered structure.[4] The functional role of such intrinsically disordered proteins is acknowledged in areas such as transcriptional regulation, translation and cellular signal transduction, where flexibility is required for such transient interactions,[5] however our understanding of their structural dynamic properties is limited.[6] These dynamic properties cannot be fully elucidated under equilibrium conditions,[7] for example, X-ray crystallography, that only provide a snapshot of the proteins frozen in crystal structures.[8] To further our understanding of structured/unstructured proteins in motion, a sophisticated system is required to measure the physical properties from which their structural dynamic behavior can be inferred. This can be achieved using a functional, ultrasensitive device able to utilize simpler model peptides,[9] with structural dynamic properties detected and measured in real-time with single-bond resolution. Model peptides present as ideal alternatives for this purpose due to the intrinsic complexity of proteins.[10]

Hence, we propose to exploit a single-peptide with an inbuilt photoswitch (cyclic peptide **1**, Figure 1a) that allows reversible interconversion between two isomers to define their structural dynamic properties. We have previously shown that photoisomerization of this peptide triggers a significant geometric change between the well-defined *cis* isomer and disordered *trans* isomer.[11] By having both isomers in the one simple model, it is possible to study their respective structural dynamic behavior in a controlled setting at the most fundamental level, which provides an appropriate model for the two protein structures described above. For device fabrication, cyclic peptide **1** will be covalently attached to nanogapped graphene electrodes to form a graphene-molecule-graphene single-molecule junction (GMG-SMJ, Figure 1b). According to our established procedures,[12] the single-molecule electronic detection method (e.g. field-effect transistor, FET) can then be used to probe the structural dynamic properties of each isomer of the peptide by transducing molecular information into quantized changes in conductance, with precise spatial control and high temporal resolution.[13] This label-free technique is ideal for investigating the structural dynamic behavior of such a photoswitchable peptide, where alternative optical and mechanical detection methods can themselves induce undesirable structural changes within the molecule.[14] When cyclic peptide **1** is bridged between the nanogapped electrodes, photoisomeri-

[*] X. Chen,[+] Prof. X. Guo
Peking-Tsinghua Center for Life Sciences, Academy for Advanced Interdisciplinary Studies, Peking University
Beijing 100871 (P. R. China)
E-Mail: guoxf@pku.edu.cn

Y. Q. Yeoh,[+] Dr. Y. He,[+] Dr. J. R. Horsley, Prof. A. D. Abell, Dr. J. Yu
ARC Centre of Excellence for Nanoscale BioPhotonics (CNBP), Institute of Photonics and Advanced Sensing (IPAS), School of Physical Sciences, The University of Adelaide
North Terrace, Adelaide SA 5005 (Australia)
E-Mail: andrew.abell@adelaide.edu.au
jingxian.yu@adelaide.edu.au

Dr. Y. He[+]
Pharmaceutical Department, Changzhi Medical College
Changzhi 046000 (P. R. China)

C. Zhou, Prof. X. Guo
Beijing National Laboratory for Molecular Sciences, State Key Laboratory for Structural Chemistry of Unstable and Stable Species, College of Chemistry and Molecular Engineering, Peking University
Beijing 100871 (P. R. China)

[+] These authors contributed equally to this work.

Supporting information and the ORCID identification number(s) for the author(s) of this article can be found under: https://doi.org/10.1002/anie.202004701.

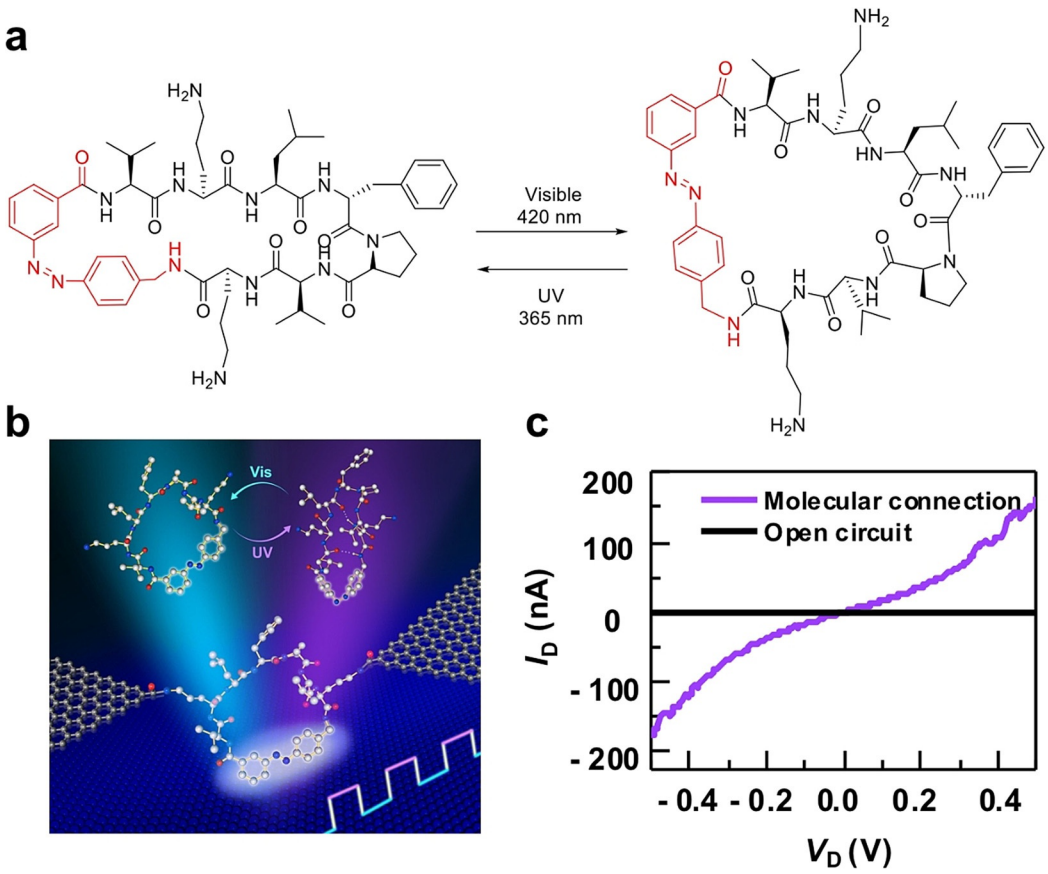

Figure 1. a) Structures of the *cis* (left) and *trans* (right) isomers of cyclic peptide **1** upon photoisomerization using light of specific wavelengths. The azobenzene photoswitch is highlighted in red. b) Schematic representation of GMG-SMJ device. c) Molecular connection test. Comparison of *I–V* curves for an open circuit (no connection, black) and molecular connection (purple), indicating the successful formation of the GMG-SMJ device.

zation of the azobenzene photoswitch is expected to result in a significant difference in electronic conductance between the two isomers due to their distinctive structures. Real-time conductance measurements on the GMG-SMJ platform enable the structural dynamic behavior of both well-defined and intrinsically disordered peptides to be revealed and compared from within the one single-peptide, thus providing important fundamental insights into this dynamic phenomenon.

Results and Discussion

Peptide Design and Device Fabrication

We have previously reported the synthesis of cyclic peptide **1** (Figure 1a).[11] ^{1}H NMR spectroscopy and lowest energy density functional theory (DFT) calculations revealed the *cis* isomer of **1** adopts a β-sheet geometry with well-defined intramolecular hydrogen bonds, while the *trans* isomer is devoid of secondary structure.[11] Detailed GMG-SMJ device fabrication and peptide coupling procedures are provided in the Supporting Information. Briefly, the free amines located on the two ornithine residues of cyclic peptide **1** were coupled to the carboxylic acid-functionalized nano-gapped graphene point contacts (Figure 1b). The fixed gap device has significant advantages over conventional STM measurements,[15] particularly as the peptide forms stable, covalent linkages to the two electrodes. This device was then characterized electronically, where the successful formation of a single-molecule junction is confirmed by a typical *I–V* curve, and an open circuit represents no peptide coupling (Figure 1c). The real-time measurements were carried out with a fixed source-drain bias voltage of 0.2 V and a sampling rate of 57.6 kSa s^{-1} at room temperature under ambient conditions. The photoinduced folding and unfolding processes in an azobenzene-containing peptide are well known[16] and occur on a picosecond timescale,[17] and thus are not the focus of this study.

Real-Time Conductance Measurements for cis and trans Isomers of Cyclic Peptide 1

To investigate the structural dynamics of cyclic peptide **1**, real-time conductance measurements were initially undertaken on the GMG-SMJ containing the *trans* isomer under dark conditions (Figure 2, *trans* 1). Within this conformation, a trimodal distribution was found, where the observed current fluctuated between three distinct states, as shown in Figures 3

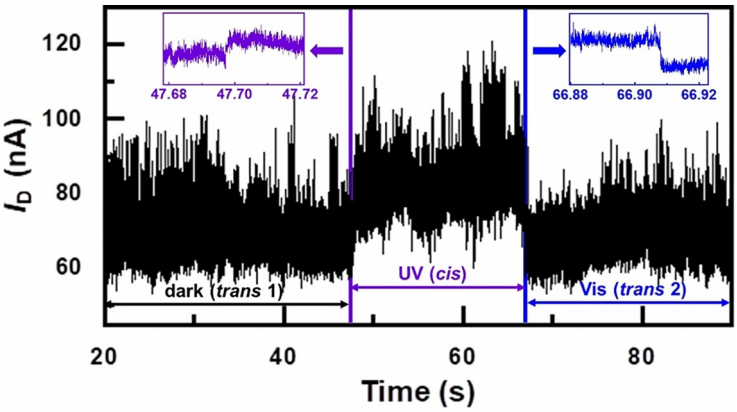

Figure 2. Real-time conductance measurements in a photoswitching cycle. Left: GMG-SMJ containing cyclic peptide **1** in its *trans* configuration (dark, *trans* 1), center: following UV irradiation (365 nm) to convert to the *cis* configuration (UV, *cis*), right: following Vis irradiation (420 nm) to convert to the *trans* configuration (Vis, *trans* 2). Insets: enlarged sections containing the relevant *I*–*t* curves upon UV irradiation (left, purple) and Vis irradiation (right, blue), showing instantaneous switching between isomers. $V_D = 0.2$ V, $V_G = 0$ V, and the sampling rate is 57.6 kSa s^{-1}.

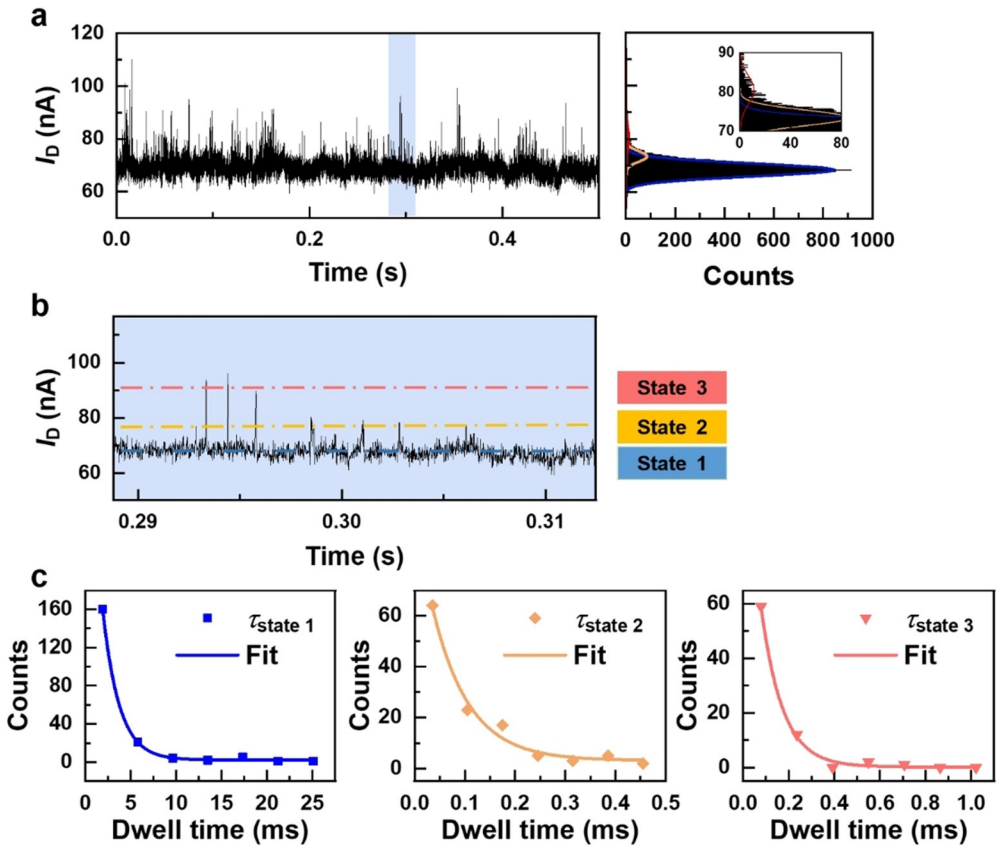

Figure 3. Real-time conductance measurements of GMG-SMJ (*trans* 1) under dark conditions with corresponding statistical analyses. a) Representative *I*–*t* trajectories of the GMG-SMJ (*trans* 1) (left) with the corresponding histogram (right). Three conductance states are observed in the *I*–*t* trajectories. The analysis of the current-count histogram shows the highest occupancy rate for low conductance state (State 1, blue), then moderate conductance state (State 2, orange), and high conductance state (State 3, red). Inset: enlarged section for States 2 and 3. b) Enlarged section of 3a showing conductance states 1–3. c) Plots of time intervals for the low (left), moderate (center) and high (right) conductance states. Dwell times (τ) were extracted from the idealized fittings of *I*–*t* curves using QuB software as shown in the Supporting Information (3.5 Kinetic analysis).

and S4. A low conductance state (State 1) was found to be the most populated, while States 2 and 3 appeared like current spikes with moderate and high conductance, respectively. The resulting current-count histogram showed three Gaussian-type fitting peaks with occupancy rates of $90.9 \pm 0.5\,\%$, $7.4 \pm 0.4\,\%$, and $1.7 \pm 0.6\,\%$, corresponding to States 1, 2, and 3,

respectively, indicating that State 1 is dominant in the *trans* isomer (Figure 3a). Figure S6d clearly shows that the noise level emanating from the device itself was approximately 1 nA, however, the difference in current between each of the three conductance states was shown to be in the order of 10 nA. This is highlighted in Figure S4, which shows all three conductance states observed over different time periods. Hence, the lower occupancy rates for State 2 and State 3 for the *trans* isomer are not deemed to be random noise, as the observed current values can clearly be discriminated from the noise. Dwell times (τ) of each state were extracted using a hidden Markov model (see Figure S7 in the Supporting Information) with time intervals obtained from QuB software,[18] while the subsequent frequency analysis demonstrated typical single exponential functions. The corresponding dwell times of the low ($\tau_{state\,1}$), moderate ($\tau_{state\,2}$) and high ($\tau_{state\,3}$) conductance states were 1.813 ± 0.083 ms, 0.073 ± 0.012 ms, and 0.094 ± 0.008 ms, respectively (Figure 3c). These data indicate that the *trans* isomer undergoes thermal fluctuations, resulting in these distinct variations in conductance.

Upon irradiation using UV light (365 nm), the overall conductance increased instantaneously indicating conversion to the *cis* isomer (Figure 2, purple inset). Detailed analysis of this dynamic process revealed that the real-time *I–t* measurements for the *cis* conformation also exhibited a trimodal current distribution, with occupancy rates of 14.3% ±0.6%, 79.5% ±0.7%, and 6.1% ±2.4% for the low, moderate, and high states, respectively (Figure 4). In contrast to the *trans* isomer, the most populated state in the *cis* isomer is the moderate conductance state (State 2). The dwell times of the three states were calculated to be $\tau_{state\,1}$ 0.883 ± 0.061 ms, $\tau_{state\,2}$ 1.067 ± 0.086 ms, and $\tau_{state\,3}$ 0.063 ± 0.002 ms corresponding to the low, moderate and high conductance states, respectively (Figure 4c). The overall conductance, occupancy rates and dwell times found for the *cis* isomer are not comparable to those of the GMG-SMJ containing the *trans* isomer, indicating that these three conductance states are clearly not a consequence of photoconversion between the isomers. As the dwell times for each state were observed to occur on a sub-millisecond timescale, and photoisomerization of azobenzene is known to occur on a picosecond timescale,[19] the conductance changes could not solely originate from the azobenzene photoswitch. In addition, to demonstrate the reversible nature of the photoswitchable device, visible light (420 nm) was used to convert the peptide to the *trans* isomer (Figure 2, *trans* **2**, blue inset). The conductance decreased instantaneously and essentially matched that of *trans* **1** (Figure S5). Covalent binding to the graphene electrodes did not appear to greatly affect the intrinsic properties of cyclic peptide **1**, with Figure S3 showing the ultrasensitive photoresponsive features that allow it to act as a light-triggered switch element. In support of the current fluctuations emanating from the photoresponse of the cyclic peptide and not from the graphene electrodes or the environment, control

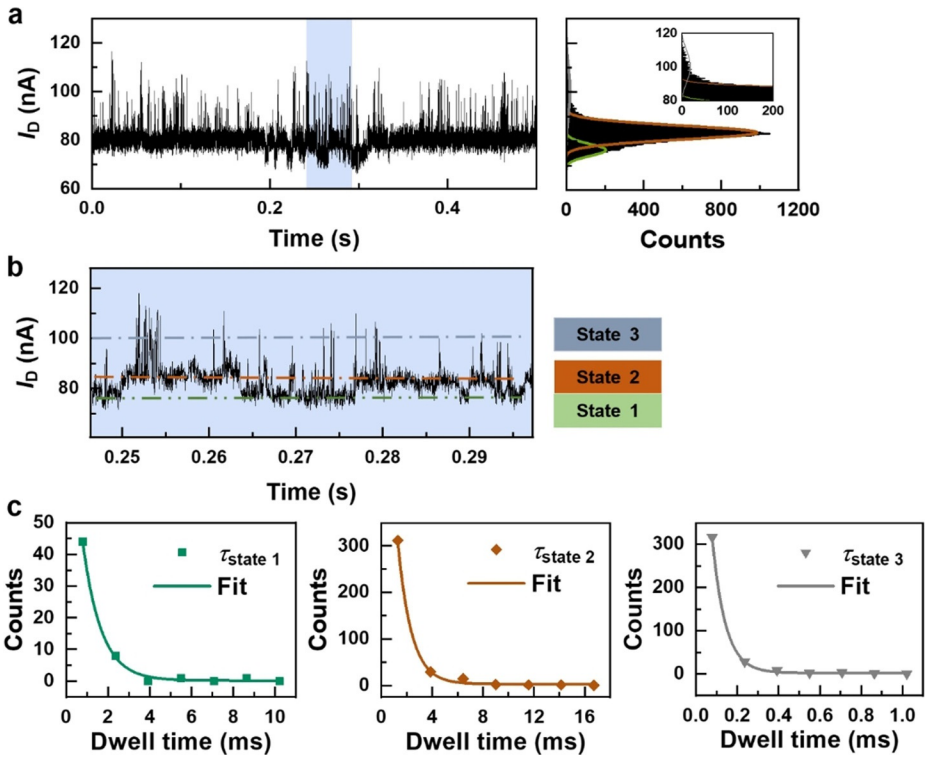

Figure 4. Real-time conductance measurements of GMG-SMJ (*cis*) under UV conditions with corresponding statistical analyses. a) Representative *I–t* trajectories of the GMG-SMJ (*cis*) (left) with the corresponding histogram (right). Three conductance states are observed in the *I–t* trajectories. The analysis of the current-count histogram shows the highest occupancy rate for the moderate conductance state (State 2, orange), then low conductance state (State 1, green), and high conductance state (State 3, grey). Inset: enlarged section for State 3. b) Enlarged section of 4a showing conductance states 1–3. c) Plots of time intervals for the low (left), moderate (center) and high (right) conductance states. Dwell times (τ) were extracted from the idealized fittings of *I–t* curves using QuB software as shown in the Supporting Information (3.5 Kinetic analysis).

experiments on partially cleaved and totally cleaved graphene devices were carried out (Figure S6). Each control experiment exhibited only one Gaussian-type fitting peak for UV, visible light, and in dark conditions. The absence of current fluctuations from these controls indicates that UV/Vis light has no observable effect on the graphene device, and hence, does not influence our results. Overall, the high temporal resolution of real-time measurements demonstrates the presence of small structural perturbations within each conformation of cyclic peptide **1**. These perturbations within each isomer may result from a negligible free energy barrier or the absence thereof, brought about by subtle movement of the peptide backbone,[20] and could provide vital information on their structural dynamics. Furthermore, the increase in conductance following UV irradiation is attributed to the distinctive β-sheet secondary structure of the *cis* isomer, which is stabilized by intramolecular hydrogen bonds. In our previous study,[21] it was reported that the formation and deformation of hydrogen bonds occurs on a submillisecond timescale in GMG-SMJs. As we observed the conductance to fluctuate between the three states of the *cis* GMG-SMJ on a submillisecond timescale (Figure 4), we postulate they are a direct consequence of the dynamic structural fluctuations that affect intramolecular hydrogen bonding. However, detailed computational studies are required to support these notions, and will be discussed in the following section.

Molecular Dynamics (MD) Simulations of GMG-SMJ

MD simulations were conducted to gain further insights into the observed structural dynamics of the GMG-SMJ. The representative snapshots of the *cis* and *trans* GMG-SMJs (Figure S10) during the course of simulations were chosen by the hieragglo algorithm-based cluster analysis using the root-mean-square (RMS) of the carbon atoms in the peptide backbone and azobenzene moiety. This was undertaken as the average frame derived from an MD run is commonly ill-defined and does not represent an appropriate chemical structure. Quantum transport simulations using DFT in conjunction with non-equilibrium Green's function (NEGF) were then performed to elucidate the difference in electronic conductance between these *cis* and *trans* GMG-SMJ snapshots. It was found that the *cis* GMG-SMJ possessed a zero-bias transmission coefficient of $3.0\times10^{-12}\,G_o$ at the Fermi level (red curve, Figure S10a), approximately two orders of magnitude higher than the *trans* GMG-SMJ ($1.0\times10^{-14}\,G_o$, black curve). Importantly, this trend is consistent with experimental observations (Figures 2 and S3). It is worth mentioning that we cannot make a direct comparison between the calculated transmission and the measured conductance, as coherent charge transport[22] and electrodes of finite cross section[23] were employed in the conductance calculations, while other incoherent processes[24] such as hopping may contribute to the conductance measurements. The Molecular Projected Self-consistent Hamiltonian (MPSH) states of the *cis* GMG-SMJ (Figure S12) exhibit a HOMO–LUMO energy gap of ≈0.612 eV, while an increased HOMO–LUMO energy gap of ≈0.688 eV is given for the *trans* GMG-SMJ. Notably, the LUMO (Figure S12) in both GMG-SMJs is localized on one of the electrodes, while the HOMO is distributed on the molecule, residing on the azobenzene moiety for the *trans* isomer, and the peptide backbone for the *cis* isomer. This indicates different roles for azobenzene and the peptide backbone in determining transmission conductance of the *cis* and *trans* isomers. Further transmission eigenchannel analysis for the *cis* GMG-SMJ showed a continuous and well-spanned electron density distribution across the entire junction (Figure S10b), indicating a higher conductance than its *trans* counterpart. The higher conductance in the *cis* GMG-SMJ is defined by the overlapping atomic orbitals from the peptide backbone, azobenzene moiety and intramolecular hydrogen bonding (Figure S10b). In contrast, the *trans* GMG-SMJ exhibited a discontinuous conduction channel (Figure S10c), with the electron density predominantly localized on the azobenzene moiety, thus resulting in an overall lower conductance. This result, together with the frontier MPSH states, indicates that the π-conjugated *trans* azobenzene plane plays a critical role in formulating the GMG-SMJ transmission eigenchannel (Figure S10c).

Hence, the MD simulation for the *trans* GMG-SMJ was further analyzed by the cluster analysis method using the dihedral angle (ϕ) between the azobenzene and graphene planes. The dihedral angle is defined by six carbon atoms. Three of these were selected from the right-side electrode to determine the graphene plane, while the azobenzene plane is defined by the other three atoms; two from the moiety and one from the peptide/graphene contacting region indicated in Figures 5a,b. The corresponding histogram of dihedral angles is depicted in Figure 5c, and the representative snapshots for each cluster were subjected to quantum transport calculations. It was found that the computed conductance oscillated in a wave form following the change in the dihedral angle (Figure 5d). Clearly, three computed conductance states (States 1–3) were identified, which are consistent with the real-time experimental conductance measurements (Figure 3), where the *trans* isomer predominantly resides in the low conductance state (State 1), with a lower population evident for moderate and high conductance states. Specifically, the computed low conductance state (State 1, green dashed line, Figure 5d) spans a broad range of dihedral angles and has the highest occupancy rate of ≈47.6% (Table S3), with $\phi\approx25°$ being the predominant species (green band, Figure 5c). The computed transmission eigenchannel for the selected device snapshot (State 1, Figure 5e) displays a discontinuous conduction channel with much lower electron density. The moderate conductance state (State 2, orange band, Figure 5c) was found at $\phi\approx-50°$ and 40°, showing the second highest occupancy rate of ≈28.6% (Table S3 and Figure 5f), while the high conductance state (State 3, blue dashed line) was found at $\phi\approx0°$, with the lowest occupancy rate of ≈23.8% (blue band, Figure 5c and Table S3). This dihedral angle ($\phi\approx0°$) allows for a better π electron alignment between the *trans* azobenzene plane and graphene electrodes, thus promoting electronic coupling between the azobenzene and the electrodes. This is evidenced by the transmission eigenchannel (Figure 5g), which shows a well-

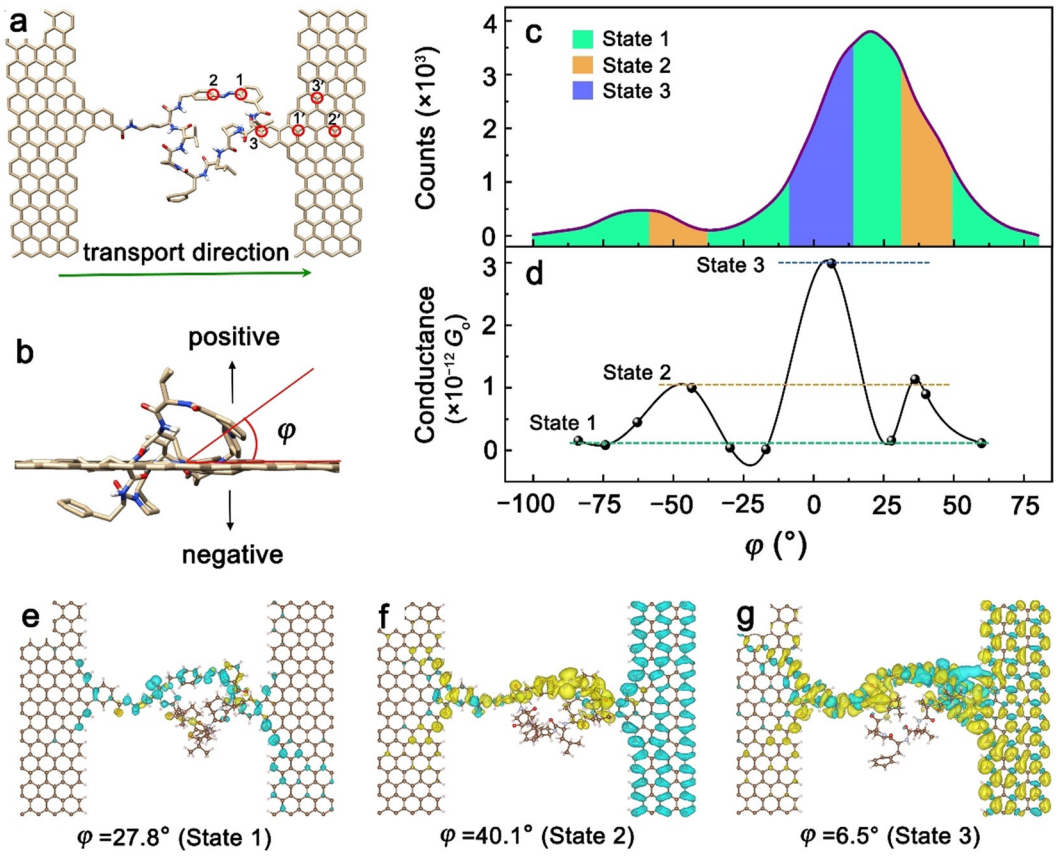

Figure 5. Conductance analyses for the *trans* GMG-SMJ MD simulation. a) Top view and b) side view of the dihedral angle (ϕ) between the azobenzene and graphene planes as defined by three atoms from each. c) Histogram (curve) of dihedral angles over the course of MD simulation, and corresponding attribution (colored bands) to the conductance states (green band = low conductance state, orange = moderate, blue = high). d) Dependence of computed conductance on dihedral angles for the selected *trans* GMG-SMJ snapshots. e–g) Computed eigenchannels of the selected GMG-SMJ snapshots with their respective dihedral angles indicated, representing the three conductance states.

spanned conductive channel with high electron density, predominantly localized on the azobenzene moiety. However, this conformation induces such a large distortion in each of the ornithine side chains, resulting in the lowest occupancy rate. The simulated conductance states and their corresponding occupancy rates concur with the real-time conductance measurements, providing clear theoretical evidence to interpret the experimental observations. Hence, these MD simulations revealed that ϕ is crucial for modulating conductance within the three discrete states found in the *trans* GMG-SMJ. While the occupancy rate is predominantly in the low conductance state for the *trans* isomer, MD simulations have shown that it can also experience higher conductance, depending on the specific orientation of the peptide within the GMG-SMJ. Notably, such variations in the dihedral angles amount to modulation of the conductance within each discrete state. The oscillation of conductance observed in Figure 5d suggests that the inherent flexibility of the *trans* isomer efficiently provides direct access to each conductance state over a wide and diverse range, depending on the orientation of the peptide. This structural dynamic behavior may potentially extend to intrinsically disordered proteins, where such structural plasticity may influence transient interactions that are readily broken and reformed, such as cellular signaling.

MD simulations showed that the *cis* isomer adopts a well-defined β-sheet secondary structure maintained by two intramolecular hydrogen bonds. Hydrogen bonding has been shown to play a significant role in electronic transport within peptides.[25] There are three possible factors affecting the conductance in the *cis* GMG-SMJ as evidenced in Figure S10b, namely (i) dihedral angle (ϕ) between the azobenzene moiety and electrode plane, (ii) hydrogen bond 1 distance (d_1), and (iii) hydrogen bond 2 distance (d_2) (Figure 6a). Hydrogen bond d_1 is defined by the CO (Leu)—NH (Orn) distance, while d_2 is defined by the CO (Val)—NH (Azo) distance. The *cis* GMG-SMJ MD trajectory was further analyzed by the cluster analysis method utilizing these three factors. In order to investigate one factor in isolation from the other two variables, representative snapshots were chosen for one, while keeping the other two parameters relatively constant. The subsequent quantum transport simulations revealed that changes in either ϕ or d_2 do not lead to a noticeable change in the computed conductance of the *cis* GMG-SMJ (Figure S13), whereas d_1 was found to be critical in determining conductance (Figure 6b). The computed conductance values are 4.5×10^{-11} G_o and 4.4×10^{-12} G_o for

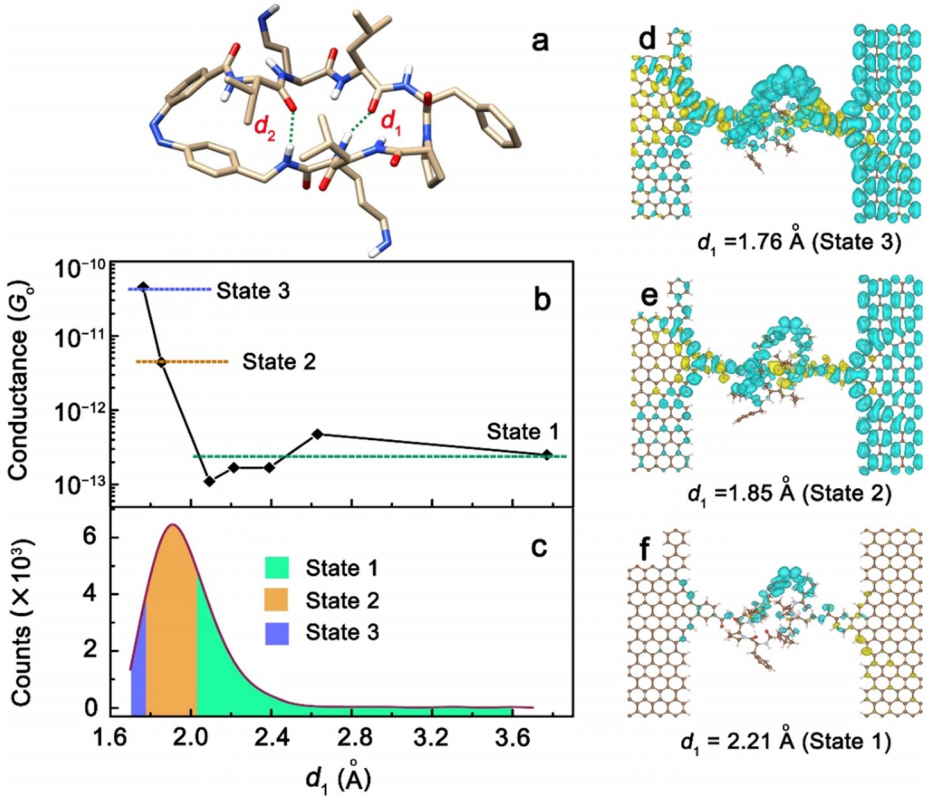

Figure 6. Conductance analyses for the *cis* GMG-SMJ MD simulation. a) Image of hydrogen bond 1 (d_1) and hydrogen bond 2 (d_2). b) Dependence of computed conductance on d_1 distance. c) Histogram (curve) of d_1 over the course of MD simulation, and corresponding attribution (colored bands) to the conductance states. d–f) Computed eigenchannels of the selected snapshots representing the low conductance state (State 1), moderate (State 2), and high (State 3).

$d_1 = 1.76$ Å and 1.85 Å respectively, while a further drop in conductance to 10^{-13} G_o was experienced when d_1 is greater than 2.10 Å (Figure 6b). The three distinct conductance states representative of d_1 shown in Figures 6d–f, are: 1.76 Å (high), 1.85 Å (moderate), and 2.21 Å (low). It was determined that the moderate conductance state (State 2) with d_1 between 1.80–2.10 Å was the predominant species (orange band, Figure 6c). Occupancy rates of ≈28.4%, ≈65.9% and ≈5.7% were found for the low, moderate, and high conductance state (States 1–3) respectively (Table S4 and Figure 6c), which also correspond with the experimental real-time measurements for the *cis* isomer (Figure 4). These three conductance states remarkably coincide with the fluctuations in d_1 as revealed by MD, thus confirming that d_1 is directly correlated to conductance. While the dihedral angle (ϕ) is crucial to the conductance in the *trans* isomer, virtually no change in conductance was found when ϕ is between −60 and 60 degrees in the *cis* isomer (Figure S13), suggesting that flexibility is not such a critical factor here. In contrast to the more flexible *trans* isomer, significant changes in conductance in the *cis* isomer can occur through the smallest of structural dynamic perturbations (sub-angstrom) within d_1. Thus, the structural dynamic properties revealed in d_1 provide new opportunities to modulate conductance within the well-defined *cis* isomer.

Despite the snapshot $d_1 = 2.21$ Å representing a strong hydrogen bond,[26] it lies in the low conductance state (State 1). It is noteworthy that Figure 6b shows two additional data points, $d_1 = 2.60$ Å (moderate hydrogen bond strength) and $d_1 = 3.80$ Å (weak hydrogen bond strength), that are also located in the low conductance state. However, when d_1 is less than 2.10 Å, the conductance increased exponentially to State 2 (moderate) and State 3 (high). These results may provide support for further investigation into the definition and interpretation of hydrogen bond strengths within a well-defined secondary structure. Collectively, this work goes beyond transducing the hydrogen bond dynamic process into real-time electronic signals, and indeed correlates the hydrogen bond lengths with their associated conductance states. These structural dynamic properties observed within d_1 of the *cis* isomer with single-bond resolution, provide crucial insights into the structural dynamic behavior of proteins that contain well-defined intramolecular hydrogen bonds needed to stabilize secondary structure.

Conclusion

Conductance measurements on a GMG-SMJ containing the photoswitchable cyclic peptide **1** revealed two distinct conformations, with an overall higher conductance observed in the *cis* isomer than for its *trans* counterpart, which is consistent with our MD simulations. This single-molecule electronic device has established itself as a robust platform to

unravel the structural dynamic properties of peptides at the molecular level. For the first time, we have unveiled three distinct conductance states which remarkably correlate to various unique structural dynamic properties within each isomer. Not only have we demonstrated modulation of conductance within this device using light, but also revealed that perturbations within both the well-defined and intrinsically disordered isomers of cyclic peptide **1** (structural dynamics) provide further capacity to manipulate conductance with precise spatial control and high temporal resolution. The *trans* isomer of cyclic peptide **1** was shown to possess a disordered configuration, while the *cis* isomer was found to contain a well-defined β-sheet secondary structure. Hence, by studying these two distinctly different isomers within one single-peptide, we have been able to provide hitherto undisclosed fundamental insights into their unique structural dynamic behavior, which may rationally extend to both intrinsically disordered proteins and those containing a well-defined secondary structure. This capacity to modulate conductance within peptides paves the way for the future design of multi-modal nanodevices with practical applications in areas such as biosensing, where such bioinspired molecular components offer a greener approach for the advancement of these technologies.

Acknowledgements

We acknowledge the National Key R&D Program of China (2017YFA0204901), the National Natural Science Foundation of China (21727806 and 21933001), the Tencent Foundation through the XPLORER PRIZE, the Australian Research Council (ARC) Discovery Project (DP180101581), the Centre of Excellence for Nanoscale BioPhotonics, Applied Basic Research Program of Shanxi Province (201701D221046), the Centre of Excellence for Nanoscale BioPhotonics (CE140100003), and Doctoral Scientific Research Foundation and Innovation Team Project of Changzhi Medical College (BS15014 and CX201904) for financial support. We also acknowledge the Australian National Fabrication Facility for providing the analytical facilities used in this work. Computational aspects of this work were supported by an award under National Computational Merit Allocation Scheme for J.Y. on the National Computing Infrastructure at the Australian National University and Pawsey Supercomputing Centre in Western Australia.

Conflict of interest

The authors declare no conflict of interest.

Stichwörter: azo compounds · nanostructures · photochemistry · proteins · single-molecule studies

[1] V. J. Vinson, *Science* **2009**, *324*, 197 – 197.
[2] P. Radivojac, L. M. Iakoucheva, C. J. Oldfield, Z. Obradovic, V. N. Uversky, A. K. Dunker, *Biophys. J.* **2007**, *92*, 1439 – 1456.
[3] J. R. Horsley, J. X. Yu, K. L. Wegener, C. Hoppmann, K. Ruck-Braun, A. D. Abell, *Biosens. Bioelectron.* **2018**, *118*, 188 – 194.
[4] M. M. Babu, R. van der Lee, N. S. de Groot, J. Gsponer, *Curr. Opin. Struct. Biol.* **2011**, *21*, 432 – 440.
[5] H. J. Dyson, P. E. Wright, *Nat. Rev. Mol. Cell Biol.* **2005**, *6*, 197 – 208.
[6] I. Nyqvist, J. Dogan, *Sci. Rep.* **2019**, *9*, 16557.
[7] U. Samuni, J. M. Friedman, *Protein-Ligand Interactions: Methods and Applications* (Ed.: G. Ulrich Nienhaus), Humana Press, Totowa, New Jersey, **2005**, pp. 287 – 300.
[8] K. Henzler-Wildman, D. Kern, *Nature* **2007**, *450*, 964 – 972.
[9] a) C. Guo, X. Yu, S. Refaely-Abramson, L. Sepunaru, T. Bendikov, I. Pecht, L. Kronik, A. Vilan, M. Sheves, D. Cahen, *Proc. Natl. Acad. Sci. USA* **2016**, *113*, 10785; b) X. Xiao, B. Xu, N. Tao, *Angew. Chem. Int. Ed.* **2004**, *43*, 6148 – 6152; *Angew. Chem.* **2004**, *116*, 6274 – 6278.
[10] J. X. Yu, J. R. Horsley, A. D. Abell, *Acc. Chem. Res.* **2018**, *51*, 2237 – 2246.
[11] Y. Q. Yeoh, J. X. Yu, S. W. Polyak, J. R. Horsley, A. D. Abell, *ChemBioChem* **2018**, *19*, 2591 – 2597.
[12] a) C. H. Gu, C. Hu, Y. Wei, D. Q. Lin, C. C. Jia, M. Z. Li, D. K. Su, J. X. Guan, A. D. Xia, L. H. Xie, A. Nitzan, H. Guo, X. F. Guo, *Nano Lett.* **2018**, *18*, 4156 – 4162; b) C. C. Jia, A. Migliore, N. Xin, S. Y. Huang, J. Y. Wang, Q. Yang, S. P. Wang, H. L. Chen, D. M. Wang, B. Y. Feng, Z. R. Liu, G. Y. Zhang, D. H. Qu, H. Tian, M. A. Ratner, H. Q. Xu, A. Nitzan, X. F. Guo, *Science* **2016**, *352*, 1443 – 1445; c) N. Xin, X. X. Li, C. C. Jia, Y. Gong, M. L. Li, S. P. Wang, G. Y. Zhang, J. L. Yang, X. F. Guo, *Angew. Chem. Int. Ed.* **2018**, *57*, 14026 – 14031; *Angew. Chem.* **2018**, *130*, 14222 – 14227; d) Y. Cao, S. H. Dong, S. Liu, L. He, L. Gan, X. M. Yu, M. L. Steigerwald, X. S. Wu, Z. F. Liu, X. F. Guo, *Angew. Chem. Int. Ed.* **2012**, *51*, 12228 – 12232; *Angew. Chem.* **2012**, *124*, 12394 – 12398.
[13] C. H. Gu, C. C. Jia, X. F. Guo, *Small Methods* **2017**, *1*, 1700071.
[14] a) S. F. Hedegaard, M. S. Derbas, T. K. Lind, M. R. Kasimova, M. V. Christensen, M. H. Michaelsen, R. A. Campbell, L. Jorgensen, H. Franzyk, M. Cardenas, H. M. Nielsen, *Sci. Rep.* **2018**, *8*, 6327; b) J. Liu, X. Huang, F. Wang, W. Hong, *Acc. Chem. Res.* **2019**, *52*, 151 – 160.
[15] B. T. Zhang, W. S. Song, P. Pang, Y. N. Zhao, P. M. Zhang, I. Csabai, G. Vattay, S. Lindsay, *Nano Futures* **2017**, *1*, 035002.
[16] a) S. H. Xia, G. Cui, W. H. Fang, W. Thiel, *Angew. Chem. Int. Ed.* **2016**, *55*, 2067 – 2072; *Angew. Chem.* **2016**, *128*, 2107 – 2112; b) F. Z. Zhang, A. Zarrine-Afsar, M. S. Al-Abdul-Wahid, R. S. Prosser, A. R. Davidson, G. A. Woolley, *J. Am. Chem. Soc.* **2009**, *131*, 2283 – 2289.
[17] J. A. Ihalainen, J. Bredenbeck, R. Pfister, J. Helbing, L. Chi, I. H. M. van Stokkum, G. A. Woolley, P. Hamm, *Proc. Natl. Acad. Sci. USA* **2007**, *104*, 5383 – 5388.
[18] C. Nicolai, F. Sachs, *Biophys. Rev. Lett.* **2013**, *8*, 191 – 211.
[19] H. M. D. Bandara, S. C. Burdette, *Chem. Soc. Rev.* **2012**, *41*, 1809—1825.
[20] E. W. Schlag, S.-Y. Sheu, D.-Y. Yang, H. L. Selzle, S. H. Lin, *Angew. Chem. Int. Ed.* **2007**, *46*, 3196 – 3210; *Angew. Chem.* **2007**, *119*, 3258 – 3273.
[21] C. Zhou, X. X. Li, Z. L. Gong, C. C. Jia, Y. W. Lin, C. H. Gu, G. He, Y. W. Zhong, J. L. Yang, X. F. Guo, *Nat. Commun.* **2018**, *9*, 807.
[22] a) Y. Imry, R. Landauer, *Rev. Mod. Phys.* **1999**, *71*, S306 – S312; b) N. Papior, N. Lorente, T. Frederiksen, A. García, M. Brandbyge, *Comput. Phys. Commun.* **2017**, *212*, 8 – 24.
[23] a) Z. H. Li, M. Smeu, S. Afsari, Y. J. Xing, M. A. Ratner, E. Borguet, *Angew. Chem. Int. Ed.* **2014**, *53*, 1098 – 1102; *Angew. Chem.* **2014**, *126*, 1116 – 1120; b) J. R. Horsley, J. Yu, A. D. Abell, *Chem. Eur. J.* **2015**, *21*, 5926 – 5933.
[24] a) M. Berritta, D. Z. Manrique, C. J. Lambert, *Nanoscale* **2015**, *7*, 1096 – 1101; b) W. M. Schosser, L. A. Zotti, J. C. Cuevas, F.

Pauly, *J. Chem. Phys.* **2019**, *150*, 174705; c) J. Yu, J. R. Horsley, A. D. Abell, *Mol. Syst. Des. Eng.* **2017**, *2*, 67 – 77.
[25] a) Y. Arikuma, K. Takeda, T. Morita, M. Ohmae, S. Kimura, *J. Phys. Chem. B* **2009**, *113*, 6256 – 6266; b) A. Shah, B. Adhikari, S. Martic, A. Munir, S. Shahzad, K. Ahmad, H.-B. Kraatz, *Chem. Soc. Rev.* **2015**, *44*, 1015 – 1027.
[26] J. M. MacLeod, F. Rosei, *Directed Assembly of Nanostructures. Comprehensive Nanoscience and Technology*, Academic Press, Cambridge, **2011**.

Manuskript erhalten: 31. März 2020
Veränderte Fassung erhalten: 15. Juli 2020
Akzeptierte Fassung online: 26. August 2020
Endgültige Fassung online: 12. Oktober 2020

